ACS OMEGA

Open Access

http://pubs.acs.org/journal/acsodf

Article

$Ti_3C_2T_x$ MXene Based Electro-Ionic Soft Actuator with Potential for Wearable Finger Straps

Huiqin Li*

Cite This: *ACS Omega* 2024, 9, 42814−42821

Read Online

ACCESS | Metrics & More | Article Recommendations | Supporting Information

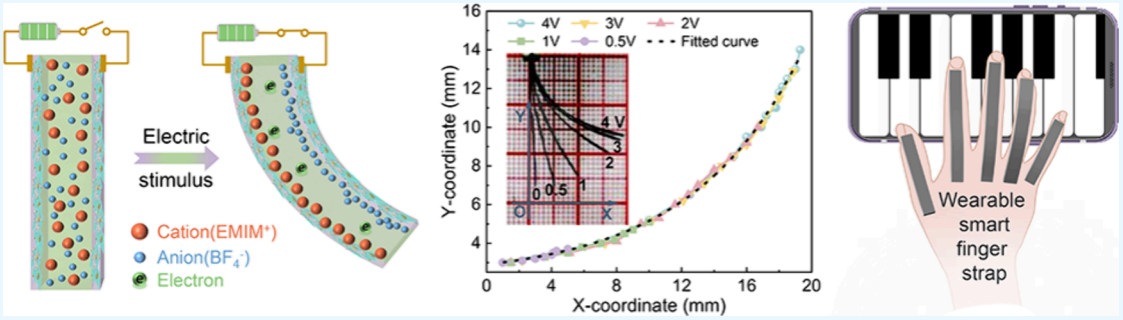

ABSTRACT: Soft electro-ionic actuators have received extensive research and attention due to their advantages such as low voltage response and adjustable deformation. However, they have not been able to enter the actual industry application like traditional rigid actuators; one of the reasons may be that the kinematic properties of actuators have been less studied. The electro-ionic actuator based on $Ti_3C_2T_x$ MXene-CNT/PPy electrode prepared in this paper shows good bending displacement (18.8 mm) and strain (0.63%) under 4 V voltage. In this article, the overlapping nature and exponential function relationship of the actuator end-point trajectories are preliminarily discussed, and the morphology change and cubic polynomial function relationship of the actuator body are considered. Moreover, in application, a novel proof-of-concept model of smart wearable finger straps is proposed. This study is a unique attempt and is hoped to provide a new research perspective in the field of soft electro-ionic actuators.

1. INTRODUCTION

Soft electro-ionic actuators, one of the electrochemical actuators, along with other types of stimulus-responsive actuators, enrich the world of soft actuators and soft robots.[1,2] Due to their advantages of light weight, convenience, large deformation under low-voltage actuation, adjustable displacement size and direction, and stable operation in air environment, they show great potential in soft robotics, wearable electronics, and micro-electromechanical systems and have attracted extensive attention from scholars at home and abroad.[3−5]

Ionic polymer−metal composite (IPMC) is a typical ionic electroactive polymer (EAP) consisting of noble metal electrodes on both sides and an intermediate electrolyte layer, which is the predecessor of the new soft electro-ionic actuator.[6,7] Limited by the shortcomings of metal electrodes that are easy to crack and high manufacturing costs, researchers have developed a new generation of conductive electrode materials with fast ion transport and ultrastorage performance, such as carbon nanotubes (CNTs),[8−11] graphene,[12−15] black phosphorus (BP),[16] $Ti_3C_2T_x$ MXene,[17,18] and metal−organic frameworks (MOFs).[19,20] In addition to innovations in materials, domestic and foreign scholars have also explored many other aspects, such as the continuous pursuit of performance indexes,[21−26] asymmetric electrodes,[27] dual-responsive electro-ionic actuators,[28,29] and more interesting application scenarios.[19,30] All these have greatly promoted the development of soft electro-ionic actuators, but there is still a lot of room to popularize electro-ionic actuators into practical applications, and more in-depth and extensive exploration is still needed urgently. Currently, few studies have been reported on the motion trajectory of the electro-ionic actuator, which is exactly the cornerstone of practical applications. There are also fewer application studies on interaction with the human body, such as wearable devices,[31,32] and most of the applications in research remain in object grasping and aesthetic display.[33−36]

Herein, a $Ti_3C_2T_x$ MXene-CNT/PPy nanostructured electrode is proposed for electro-ionic soft actuators. The described electrode combines the characteristics of double-layer capacitance and pseudocapacitance, which makes the actuator have good electrochemical and actuation performances. This work is also the first preliminary attempt to explore the kinematic

Received: May 15, 2024
Revised: August 3, 2024
Accepted: September 3, 2024
Published: October 10, 2024

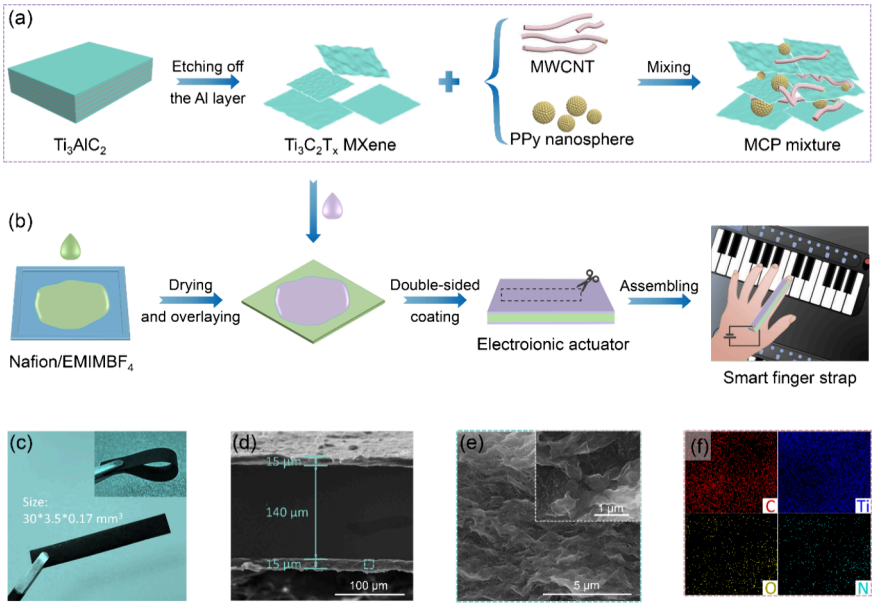

Figure 1. Schematic preparation and morphological characterization of the designed electro-ionic actuator. Schematic diagram for fabrication of (a) MCP mixture and (b) electro-ionic actuator. (c) Optical images of the actuator. SEM images of (d) A-MCP10 cross-section and (e) MCP10 electrode cross-section and its magnification. (f) Energy-dispersive spectra analysis on MCP10 electrode.

properties of this type of actuator, laying the foundation for more in-depth practical applications. Finally, the actuator is applied to a wearable finger strap, and it is expected to provide help for patients with hand disorders in the future in three dimensions, ranging from rehabilitation exercises to gestures when interacting with others to playing the piano.

2. EXPERIMENTAL METHODS

2.1. Materials and Reagents. Ti_3AlC_2 (MAX, 400 mesh) powder and a polypropylene membrane (celgard 3501, 0.25 μm in pore size) were purchased from Jilin 11 Technology Co., Ltd. (Jilin, China). Hydrochloric acid (HCl), *N*,*N*-dimethylformamide (DMF), and *N*,*N*-dimethylacetamide (DMAc) were obtained from Sinopharm Chemical Reagent Co., Ltd. (Shanghai, China). Lithium oxide (LiF) and 1-ethyl-3-methylimidazolium tetrafluoroborate (EMIMBF$_4$) were provided by Shanghai Aladdin Biochemical Technology Co., Ltd. (Shanghai, China). Multiwalled carbon nanotubes (MWCNTs) were purchased from Suzhou Tanfeng Graphene Technology Co., Ltd. (Suzhou, China). Polypyrrole (PPy, 20 wt % loading, composite with carbon black) and Nafion-H Perfluorinated resin (Nafion) were purchased from Shanghai Macklin Biochemical Co., Ltd. (Shanghai, China). All the above-mentioned chemicals were used without any further purification.

2.2. Synthesis of $Ti_3C_2T_x$ MXene Single Few-Layer Nanosheets. The detailed processes of preparing $Ti_3C_2T_x$ (T_x = −O, −OH, −F) nanosheets can be found elsewhere by in situ HF etching method to selectively etch the Al layer from precursor Ti_3AlC_2.[1] In short, 3 g of LiF was mixed with 60 mL of 9 M HCl to form an etchant, and 3 g of Ti_3AlC_2 was etched for 24 h; then, the reaction solution was washed with deionized water multiple times until the pH value reached 6. Lastly, the solution was sonicated at 360 W for 4 h and then centrifuged at 4000 rpm for 10 min to obtain the supernatant, which was a single few-layer $Ti_3C_2T_x$ nanosheets.

2.3. Preparation of the MCP Mixture and MCP Film. PPy powder was dispersed into DMF, and the PPy dispersion was obtained after sonication and stirring. Carbon nanotube (CNT) aqueous solution with a small amount of dispersant added was stirred, ultrasonically treated, and centrifuged at 3500 rpm for 5 min to obtain the uniform CNT dispersion. The single few-layer $Ti_3C_2T_x$ nanosheet colloidal solution, the CNT dispersion and the PPy dispersion were mixed thoroughly to form a mixed solution, which is called MCP solution. The MCP solution was then filtered by using a vacuum-assisted filtration device and a celgard 3501 filter membrane to yield the MCP film. Maintaining a mass ratio of $Ti_3C_2T_x$ to CNT of 10:1, and on this basis, films comprising 0%, 5%, 10%, 15%, and 20% of PPy, denoted as MCP0, MCP5, MCP10, MCP15, and MCP20, were made.

2.4. Fabrication of Electro-Ionic Actuator. Nafion (1 g) and EMIMBF$_4$ (0.7 g) were added to 10 mL of DMAc and then stirred at 45 °C for 24 h. 4 mL of the obtained solution was uniformly poured on the substrate and fully dried at 80 °C to obtain the ionic polymer film.[19,20,27] On both sides of the ionic polymer, the MCP mixture was coated evenly and dried completely at 60 °C. The specific mass of the MCP mixture is 30 mg of $Ti_3C_2T_x$ and CNT (mass ratio 10:1), and 0 mg/1.5 mg/3 mg/4.5 mg/6 mg of PPy (corresponding to MCP0/MCP5/MCP10/MCP15/MCP20 in turn). After one side was dried, the other side was coated to obtain a sandwich-type film. The film was then cut into a regular long strip to obtain an electro-ionic actuator.

2.5. Instruments and Characterization. The morphologies of samples were observed by using scanning electron microscopy (SEM, Inspect F50, FEI). The chemical compositions and crystal structures of samples were characterized by using X-ray diffraction (XRD, Ultima IV, Rigaku), a Raman spectrum (RAM-PRO-785E, Agiltron), and X-ray photoelectron spectroscopy (XPS, K-Alpha, Thermo Scientific). The electrical conductivity was tested with a four-probe resistivity meter (HPS2662, Helpass). The electrochemical characterization was carried out on an electrochemical workstation (CHI660E, Shanghai Chenhua Instruments). In the electrochemical test, the dimension of the electrode sample was 30 × 5 mm^2, and the length of the sample immersed in 1 M sulfuric acid

https://doi.org/10.1021/acsomega.4c04647
ACS Omega 2024, 9, 42814−42821

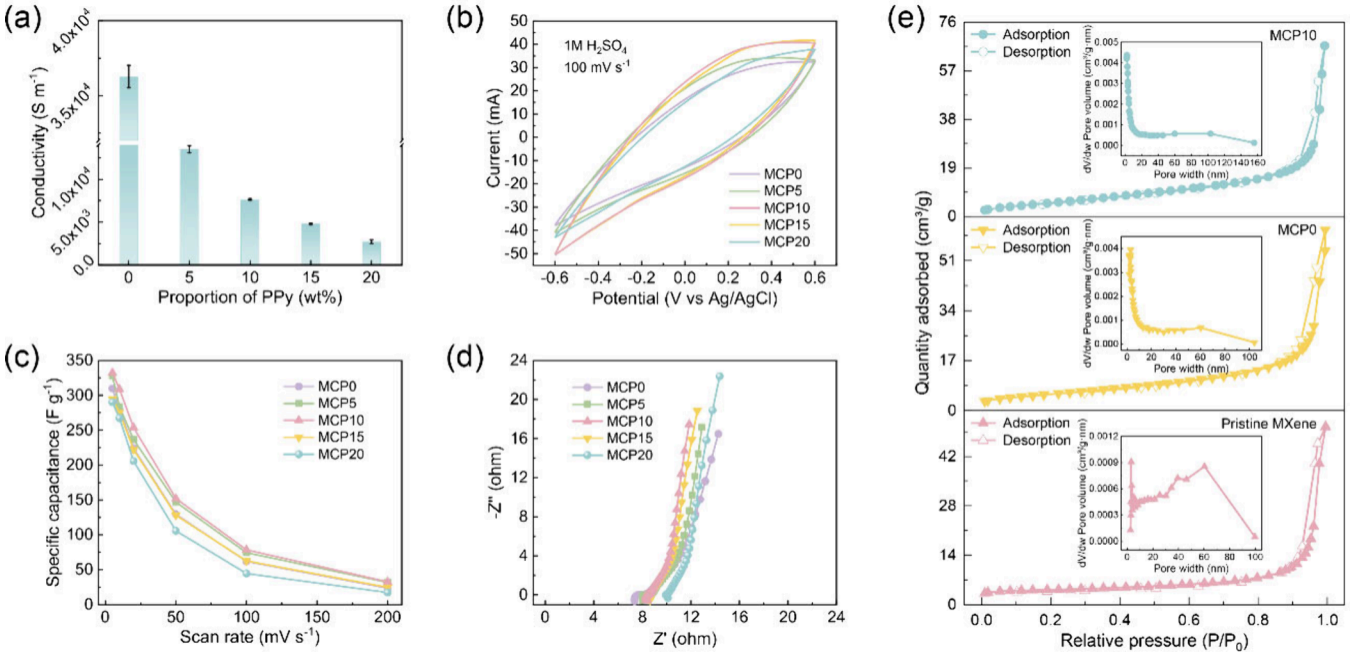

Figure 2. Conductivity, electrochemical and specific surface area testing of MCP electrode films. (a) The conductivities, (b) the cyclic voltammograms in −0.6 to +0.6 V, (c) specific capacitance values at various scan rates, and (d) Nyquist plots of MCP electrodes. (e) Nitrogen adsorption−desorption isotherms and the corresponding BJH pore size distribution curves (inset) of pristine MXene, MCP0, and MCP10 electrodes.

solution was 21.5 mm. The surface area property was analyzed using a Brunner-Emmett-Teller (BET) surface area analysis (TriStar II 3020, Micromeritics instrument). A direct current regulated power supply (WYJ-2A/0−15 V, Quanli) and a signal generator (DG1022Z, Rigol) were used to output DC and AC voltage, respectively. The actuation process of the electro-ionic actuator was monitored with a camera (EOS M6 II, Canon). The bending displacements were analyzed by using Adobe Premiere Pro CC 2018 and Adobe Photoshop CS6. The temperature variation was monitored with an infrared camera (343, Fotric). The blocking force was tested by a force-measuring platform system (including Charge amplifier type 5018, Kistler). Specifically, in the bending displacement and blocking force tests, the dimension of the actuator sample was 30 × 3.5 mm^2, the free length remaining after one end of the actuator was clamped by the alligator clip was 27 mm, and the test voltage range was 0.5−4 V.

3. RESULTS AND DISCUSSION

3.1. Fabrication Strategy and Characterizations of the MCP-Based Electro-Ionic Actuator. For electro-ionic actuators, the actuation mechanism is essentially caused by the migration of anions/cations in the electrolyte. Still, it can be subdivided into pseudocapacitive actuation and electric double-layer capacitive actuation depending on the materials used in the electrode layer.[3] If the electrode material belongs to pseudocapacitive materials, such as MnO_2,[37] polyaniline (PANI),[6] and polypyrrole (PPy),[38,39] it is due to the redox reaction that leads to electron gain and loss, which causes anion/cation migration to ensure electroneutrality. If the electrode material belongs to the electric double-layer capacitive materials, such as CNTs, MXene and MOFs, then it is due to electrostatic-induced anion/cation adsorption onto the porous surface. For the electrode material in this article, the combination of typical electric double-layer capacitive materials ($Ti_3C_2T_x$ MXene and MWCNTs) and representative pseudocapacitive material (PPy) is selected, as shown in Figures 1a and S1. Among them, CNTs can be intercalated into the MXene lamellae to prevent their stacking and ensure high electrode conductivity, and PPy nanospheres can also increase the electrochemical performance of the overall electrode through redox reactions while assisting intercalation. The intermediate electrolyte layer is, as in many pieces of literature, a hybrid membrane of semipermeable ionic-exchange polymerelectrolyte (Nafion) with ionic liquid (1-eutyl-3-methylimidazolium tetrafluoroborate, $EMIMBF_4$). The sandwich-type electro-ionic actuator prepared accordingly, after cutting and assembling, can be used as a conceptual demonstration model for smart wearable finger straps (Figure 1b).

From the appearance, the prepared actuator appears as a long black strip and has good flexibility (Figure 1c). Microscopically, the actuator has a clear three-layer structure, with the middle layer being much thicker than the electrode layer, and the three layers are tightly bonded without gaps (Figure 1d). From the microscopic view of the electrode, $Ti_3C_2T_x$ MXene sheet layers were successfully intercalated, forming an obvious porous folded morphology, and the main component elements were evenly distributed (Figure 1e,f). To ensure a certain conductivity, on the basis of maintaining 10 wt % CNT,[40] electrode films containing 0%, 5%, 10%, 15%, and 20% PPy were prepared, respectively, named MCP0, MCP5, MCP10, MCP15, and MCP20 (see the experimental section in the Supporting Information for detailed preparation method). The cross-sectional morphology of each electrode film is shown in Figure S2, and a gradual increase in intercalation content can be observed at the same scale. Meanwhile, the analysis of X-ray diffraction (XRD) patterns, Raman spectroscopy, and X-ray photoelectron spectroscopy (XPS) all prove the successful preparation of the $Ti_3C_2T_x$ MXene-CNT/PPy electrode film (Figures S3 and S4).

3.2. Multiple Properties of MCP Electrode Films. The properties of the electrode film have a great relationship with the

https://doi.org/10.1021/acsomega.4c04647
ACS Omega 2024, 9, 42814−42821

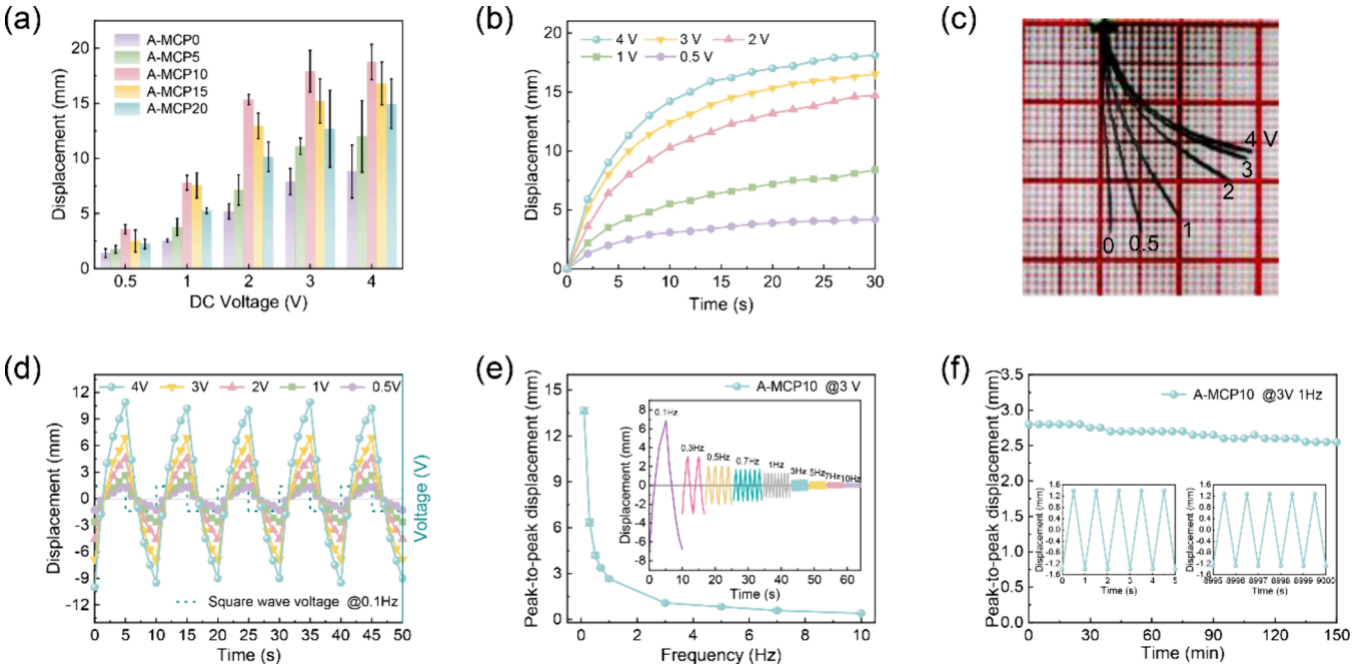

Figure 3. Actuation performances of the designed actuators. (a) Response displacements of actuators under DC voltage from 0.5 to 4 V. (b) Time-dependent bending displacements and (c) the physical bending image of A-MCP10. (d) Bending displacements over time of A-MCP10 under square wave voltage at 0.1 Hz. (e) peak-to-peak displacements of A-MCP10 at frequencies from 0.1 to 10 Hz under square wave voltage of 3 V. Inset: actuation displacements with increasing frequencies. (f) Actuation stability test of A-MCP10 under square wave voltage of 3 V at 1 Hz. Inset curves show the first five cycles and the last five cycles of actuation performance.

overall driving performance of the actuator. First, in terms of conductivity, it gradually decreases as the PPy content increases because PPy itself does have poorer conductivity than $Ti_3C_2T_x$ MXene and CNTs. However, the conductivity remains on the order of 10^3 S m^{-1}, which still satisfies the electrode's need for conductivity (Figure 2a). In addition, cyclic voltammetry (CV) and electrochemical impedance spectroscopy (EIS) tests were performed on the MCP electrode films in a three-electrode system. CV curves at various rates show that MCP electrodes can be used as anode and cathode materials stably and reversibly. At high scan rates, the curves have no significant peak, disclosing the electric double-layer capacitance characteristic of the MCP electrode, whereas at low rates, especially for MCP20 at 5 mV s^{-1}, display slight redox peaks, manifesting the added pseudocapacitance characteristic of the MCP electrode due to the presence of PPy (Figures 2b and S5). Moreover, it was calculated (see the calculation section in Supporting Information for details) that the specific capacitance of the MCP electrode increases first and then decreases with the increase of PPy content (numerically, MCP0 < MCP5 < MCP10, and MCP10 > MCP15 > MCP20), and the MCP10 electrode exhibits the maximum specific capacitance at all rates (Figure 2c). The specific capacitance of MCP10 is 332 F g^{-1} when the scan rate is 5 mV s^{-1}. In the Nyquist diagram, the MCP electrode is almost straight in the low-frequency region, and the slope of the straight line is the largest for the MCP10 electrode (Figure 2d). This demonstrates that the MCP10 electrode has a more desirable capacitance performance, which is conducive to the diffusion and transport of ions. The reason for the good electrochemical performance of the MCP10 electrode is in addition to the high conductivity, the synergistic effect of pseudocapacitance and electric double-layer capacitance, but also the 3D network structure with a larger ion-accessible surface area. The nitrogen adsorption−desorption isotherms reveal that the MCP10 electrode has a larger specific surface area than the MXene electrode, specifically, 21.76 m^2 g^{-1} (Figure 2e). Meanwhile, the average pore size is 15.80 nm, and in contrast, there are more meso- and micropores with apertures less than 4 nm, which not only facilitates the ion diffusion and enhances the capacitance but also plays a positive role in the electrode volume expansion.[41] Therefore, it can be predicted that the electro-ionic actuator based on the MCP10 electrode will show good driving displacement.

The MCP electrode is mainly based on two effects: 1) Electric double-layer capacitance effect: The electric double-layer capacitance is mainly related to the porous structure. The lamellar MXene is easy to stack, but after the introduction of CNT intercalators, the stacking of MXene is inhibited, which makes the specific surface area increase and is conducive to ion adsorption. This effect is more optimized after introducing both CNT and PPy intercalators. 2) Pseudocapacitance effect: The pseudocapacitance is mainly related to the redox reaction. PPy, as a typical conductive polymer, can undergo redox reactions, causing electron gain and loss in the polymer chain. After the introduction of PPy, the electrochemical performance is better. Overall, the introduction of appropriate amounts of CNT and PPy into MXene is mainly from the perspective of improving the electric double-layer capacitance and pseudocapacitance, respectively. The synergistic effect of the three can lead to a good response performance of the actuator.

3.3. Actuation Performance of Electro-Ionic Actuators.

For ease of description and writing, the electro-ionic actuators based on MCP0, MCP5, MCP10, MCP15 and MCP20 electrodes are denoted as A-MCP0, A-MCP5, A-MCP10, A-MCP15, and A-MCP20, respectively. The mechanical properties of these MCP-based actuators can be evaluated by tensile testing, as shown in Figure S6. These actuators are fixed at one end and free at the other end, with the left and right sides of the

https://doi.org/10.1021/acsomega.4c04647
ACS Omega 2024, 9, 42814−42821

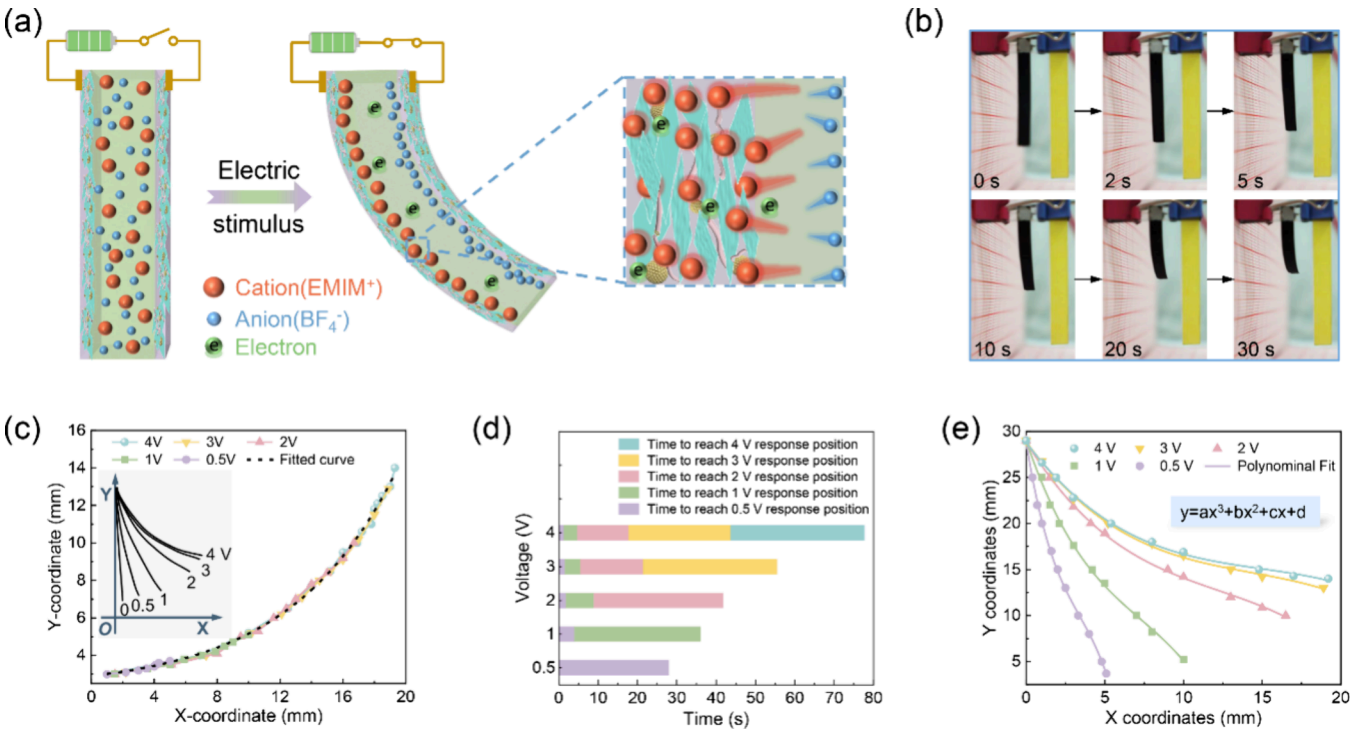

Figure 4. Actuation mechanism and kinematic properties of the designed actuator. (a) Schematic diagram of the actuation mechanism. (b) Side view of the motion of A-MCP10 at 3 V DC voltage. (c) The 2D trajectory of the end-point of the actuator in the main view. (d) Time for the actuator to reach the steady-state response position at different DC voltages. (e) 2D morphology fitting plots of the steady-state response of the whole actuator under different voltages.

fixed end energized to test their response performances under DC and AC voltages. At a small DC voltage of 0.5 V, the actuators already have an obvious bending displacement, which gradually increases as the applied voltage increases. The A-MCP10 consistently exhibits the largest bending displacement, which was up to 18.8 mm with a bending strain of 0.63% at 4 V DC voltage (Figures 3a and S7a). However, it is not possible to increase the voltage without limitation to achieve greater bending displacement and strain since too much voltage will cause the actuator to burn out, so the driving voltage in this work is limited to less than 4 V. In detail, the actuator can quickly sense the voltage input and start to respond and reach the response steady state in about 30 s (Figure 3b). The steady-state response graph is shown in Figure 3c. Under AC voltage, the actuator can be actuated in both left and right directions because the change in voltage direction directly affects the migration direction of ions in the electrolyte, which then changes the actuation direction of the actuator. Moreover, the bending displacement of the actuator under square wave voltage is better than that under sinusoidal voltage, because the square wave voltage induces more anion/cation migration over the same period (Figures 3d and S7b). In addition, the peak-to-peak displacement attainable by the actuator decreases with increasing excitation frequency (0.1−10 Hz), as indicated more clearly in the inset due to the severe lack of time required for ion migration at high frequencies (Figure 3e). Cyclic stability testing of A-MCP10 shows that the actuator has good durability, maintaining 91.1% of the initial bending displacement after 150 min (Figure 3f). Good reproducibility is also found for different batches of electro-ionic actuators (Figure S8). Furthermore, the energy transduction efficiency of A-MCP10 at different frequencies is also calculated, up to 1.47% (Figure S9). In general, the designed actuator exhibits good driving performance and stability compared to other electro-ionic actuators (Table S1), which is mainly attributed to the designed MCP electrode that provides excellent and stable transport paths for ion migration and charge transfer.

3.4. Actuation Mechanism and Kinematic Properties of the Electro-Ionic Actuator. The actuation mechanism of A-MCP is shown in Figure 4a. Under the applied electric field, cations (large ion molecules) and anions (small ion molecules) in the ionic liquid (IL) in the Nafion electrolyte membrane migrate toward the cathode and anode sides, respectively.[18] Two effects drive this migration action: on the one hand, the double electric layer effect, where the high porosity and micro/mesopores of the electrode membrane can promote the adsorption of ions on the electrode surface and inside; on the other hand, the pseudocapacitance effect, where the redox reaction of PPy at the electrode provides additional charge transfer, improves the ion storage capacity, and allows more ions to be embedded in the electrode. This synergistic effect induces sufficient ion migration, and owing to the size difference of the anion/cation itself, the expansion of the cathode will be more significant than that of the anode, eventually causing the actuator to bend significantly toward the anode.[6]

According to the above actuation mechanism, the motion of the actuator should theoretically be planar two-dimensional under the premise of ignoring manufacturing errors. From the side view and main view of the actuator during motion, it can be observed relatively intuitively (Figure 4b,c). In the main view, after establishing a Cartesian coordinate system, as shown in the inset in Figure 4c, the end-point of the actuator is taken as the research object, and it is found that its trajectories under different voltages overlap and can be represented by the same exponential function. The specific expression is shown in Table S2. Specifically, the motion trajectory of the actuator at 4 V paths

https://doi.org/10.1021/acsomega.4c04647
ACS Omega 2024, 9, 42814−42821

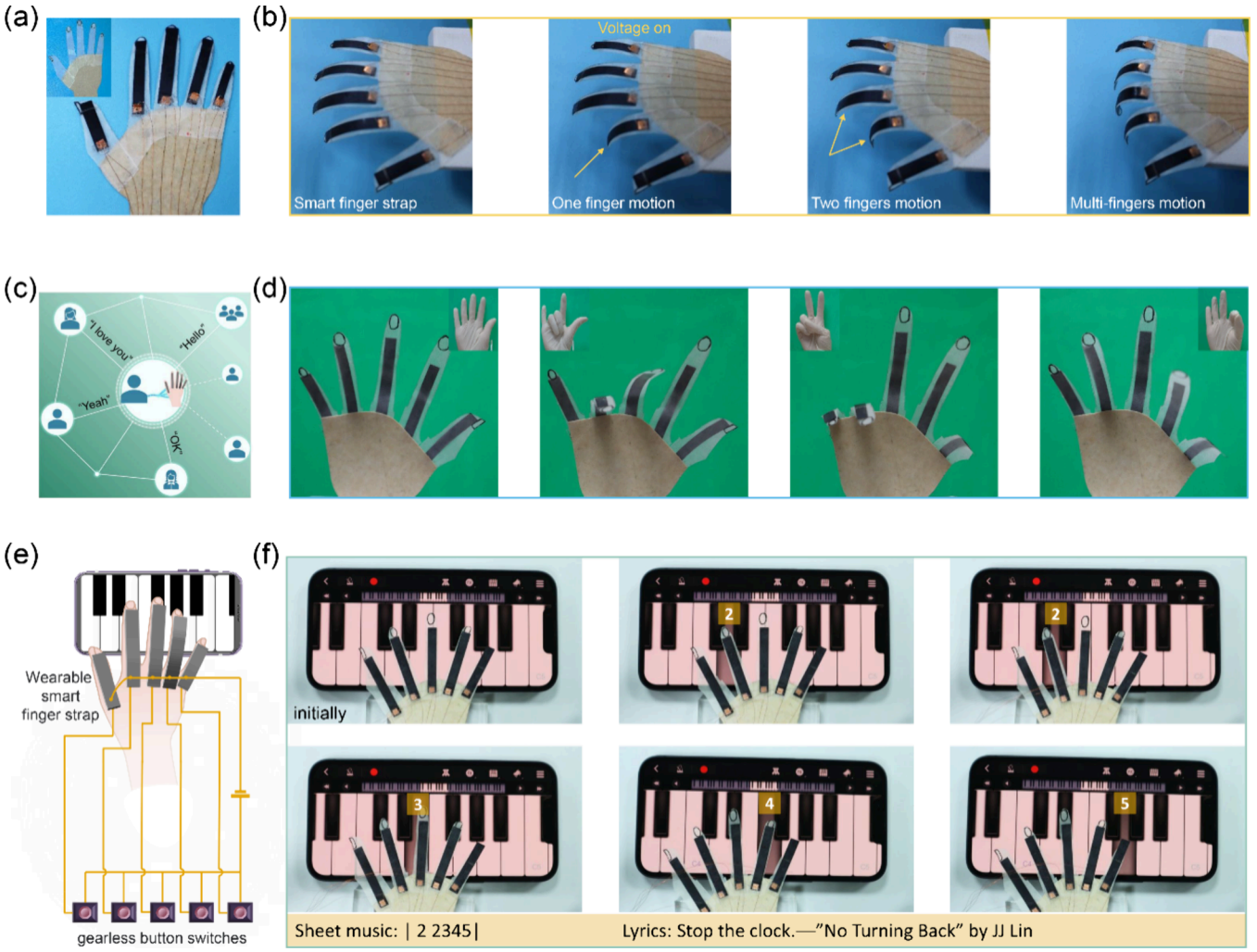

Figure 5. Applications of the designed electro-ionic actuator. (a) Optical image of the wearable smart finger strap (inset is before installation). (b) Smart finger strap aids in rehabilitation. (c) Schematic and (d) physical drawings of smart finger straps assisting in gestural interaction when communicating with people. (e) Schematic and (f) physical drawings assisting in playing the electronic piano.

through trajectories at 3, 2, 1, and 0.5 V; the trajectory of the actuator at 3 V paths through trajectories at 2, 1, and 0.5 V, and so on (Figure 4c). It is just that the time for the actuator to reach the steady-state response position of 2, 1, and 0.5 V is different at 4 V versus 3 V, and the higher the voltage, the shorter the time used. As shown in Figure 4d, taking 4 V as an example, the time taken by the actuator to reach the steady state position of 3, 2, 1, and 0.5 V is accelerated by 8, 20, 28.5, and 26.8 s, respectively, compared with that at the original voltage. Furthermore, the morphology change of the actuator body throughout the motion process is recorded, and it is found upon fitting that it can always be expressed by the same type of equation, i.e., a cubic polynomial (Figure 4e). The exact values are listed in Table S3.

The above exposition of the kinematic properties of the actuator is universal and equally applicable to other film-type soft actuators. Solving the end-point trajectory of the rigid actuator is fundamental and important in traditional rigid-body robots,[42,43] but the current research related to the motion trajectories of soft actuators is still relatively scarce, which may be a factor restricting soft actuators moving toward practical applications. soft actuators, compared to rigid actuators, need to consider the changes in the actuator body during motion in addition to focusing on the end-point trajectory. We have performed a very preliminary and tiny exploration here.

3.5. Application of Actuators to Wearable Finger Strap Models and Their Pros and Cons. Based on the good bending motion of the actuator and to expand the application of electro-ionic actuators, a proof-of-concept model of smart wearable finger straps is designed and fabricated. As shown in Figure 5a, on top of the hand model made of paper, an actuator is tied to each finger and each actuator is guaranteed to have good electrical contact separately. When energized, the smart finger straps can move with the fingers to achieve single, two, and multifinger dexterity movements, which has potential applications in helping the rehabilitation of patients with hand disorders (Figure 5b). At the same time, the assisting role of gestures is often indispensable when people communicate with each other. The smart finger strap can also be used to carry the fingers to make various gestures, such as "Hello", "I love you", "Yeah", and "OK" (Figure 5c,d). In addition, it has the potential to help people with hand disorders regain hope and add joy to their lives, such as playing the electronic piano on a smartphone. When the actuator is energized, it gradually bends downward to contact the screen and reaches a sufficient contact area to trigger the piano keys. Because the smartphone screen has a strong

https://doi.org/10.1021/acsomega.4c04647
ACS Omega 2024, 9, 42814−42821

penetrating power, the trigger operation is not affected even if it is separated by the finger model (a layer of weighing paper). The connection schematic and physical diagrams of each device are shown in Figures 5e and S10, with each finger strap being independently controlled by a gearless button switch. The successful interaction of an actuator and a "finger" wearing an actuator with the electronic piano is demonstrated in Figure S11 and Video S1. Interestingly, the wearable smart finger straps can carry the finger model to play a melody from J. J. Lin's "No turning back", as shown in Figure 5f and Video S2. These promising results demonstrate the potential of electro-ionic soft actuators to help people with hand disorders from multiple perspectives in the future.

Although electro-ionic actuators have many advantages for wearable finger straps, such as compatibility with human skin as well as lightweight and convenience (compared to rigid actuators), safe operating voltage (compared to dielectric elastomer actuators), suitable operating temperature (compared to photothermal and electrothermal actuators) (Figure S12), no noise (compared to fluid-driven actuators), and independence from ambient humidity (compared to humidity actuators). Admittedly, the blocking forces of the currently reported electro-ionic actuators are still relatively low, and the maximum blocking force of the actuator in this paper is only 43 mN (Figure S13). In the future, the blocking force can be improved by improving the stiffness of the material under the condition of ensuring bending performance,[44] or by superimposing multiple actuators,[19] or by combining with a multistage force amplification mechanism.[45] Currently, there are fewer specialized studies on the blocking force of electro-ionic actuators, which deserves the attention of researchers.

4. CONCLUSIONS

In summary, this study presents an electro-ionic actuator based on $Ti_3C_2T_x$ MXene-CNT/PPy electrode with displacements and strains of 18.8 mm and 0.63% at 4 V voltage. The kinematic properties of the actuator are preliminarily explored by fitting the end-point trajectory and the body trajectory of the actuator under different voltages. The conceptual demonstration model of smart wearable finger straps is proposed to expand the application scenario of interaction between the electro-ionic actuator and the human body. The research in this paper is a tentative exploration, hoping to provide a new research perspective for realizing the controllable interaction of electro-ionic actuators with the human body.

■ ASSOCIATED CONTENT

Supporting Information

The Supporting Information is available free of charge at https://pubs.acs.org/doi/10.1021/acsomega.4c04647.

Related calculation formulas, SEM images, XRD, Raman, and XPS spectra and corresponding analyses, cyclic voltammetry test diagrams, mechanical performance data, bending strain data, displacement curves under sinusoidal voltage, reproducibility of different batches, energy conversion efficiency data at different frequencies, on-site experimental diagram when playing the electronic piano on a smartphone, diagram of the simple interaction of an actuator and a "finger" with the electronic piano, infrared thermal image and temperature change curve, blocking force test schematic diagram and blocking force data curve, actuation performance comparison table, specific data tables for the fitted curves (PDF)

Video S1: successful interaction of an actuator and an actuator-wearing "finger" with the electronic piano on a smartphone (MP4)

Video S2: smart wearable finger straps in assisting a hand model to play a melody on a smartphone (MP4)

■ AUTHOR INFORMATION

Corresponding Author

Huiqin Li − *School of Mechanical Engineering, Southeast University, Nanjing 211189, People's Republic of China;* orcid.org/0009-0007-0848-6198; Email: lhq130115@163.com

Complete contact information is available at: https://pubs.acs.org/10.1021/acsomega.4c04647

Notes

The author declares no competing financial interest.

■ ACKNOWLEDGMENTS

This work was financially supported by Prof. Lei Liu's group at the School of Mechanical Engineering, Southeast University.

■ REFERENCES

(1) Wu, G.; Hu, Y.; Liu, Y.; Zhao, J.; Chen, X.; Whoehling, V.; Plesse, C.; Nguyen, G. T. M.; Vidal, F.; Chen, W. Graphitic Carbon Nitride Nanosheet Electrode-Based High-Performance Ionic Actuator. *Nat. Commun.* **2015**, *6* (1), 7258.

(2) Wen, J.; Zhou, L.; Ye, T. Polymer Ionogels and Their Application in Flexible Ionic Devices. *SmartMat* **2024**, *5* (2), No. e1253.

(3) Zhu, X.; Hu, Y.; Wu, G.; Chen, W.; Bao, N. Two-Dimensional Nanosheets-Based Soft Electro-Chemo-Mechanical Actuators: Recent Advances in Design, Construction, and Applications. *ACS Nano* **2021**, *15* (6), 9273−9298.

(4) Li, J.; Ma, W.; Song, L.; Niu, Z.; Cai, L.; Zeng, Q.; Zhang, X.; Dong, H.; Zhao, D.; Zhou, W.; Xie, S. Superfast-Response and Ultrahigh-Power-Density Electromechanical Actuators Based on Hierarchal Carbon nanotube Electrodes and Chitosan. *Nano Lett.* **2011**, *11* (11), 4636−4641.

(5) Asaka, K.; Mukai, K.; Sugino, T.; Kiyohara, K. Ionic Electroactive Polymer Actuators Based on Nano-Carbon Electrodes. *Polym. Int.* **2013**, *62* (9), 1263−1270.

(6) Liu, Q.; Liu, L.; Xie, K.; Meng, Y.; Wu, H.; Wang, G.; Dai, Z.; Wei, Z.; Zhang, Z. Synergistic Effect of A r-GO/PANI Nanocomposite Electrode Based Air Working Ionic Actuator with A Large Actuation Stroke and Long-Term Durability. *J. Mater. Chem. A* **2015**, *3* (16), 8380−8388.

(7) Ahn, J.; Gu, J.; Choi, J.; Han, C.; Jeong, Y.; Park, J.; Cho, S.; Oh, Y. S.; Jeong, J. H.; Amjadi, M.; Park, I. A Review of Recent Advances in Electrically Driven Polymer-Based Flexible Actuators: Smart Materials, Structures, and Their Applications. *Adv. Mater. Technol.* **2022**, *7* (11), 2200041.

(8) Kim, J.; Bae, S. H.; Kotal, M.; Stalbaum, T.; Kim, K. J.; Oh, I. K. Soft but Powerful Artificial Muscles Based on 3D Graphene-CNT-Ni Heteronanostructures. *Small* **2017**, *13* (31), 1701314.

(9) Kong, L.; Chen, W. Carbon Nanotube and Graphene-Based Bioinspired Electrochemical Actuators. *Adv. Mater.* **2014**, *26* (7), 1025−1043.

(10) Wu, G.; Li, G. H.; Lan, T.; Hu, Y.; Li, Q. W.; Zhang, T.; Chen, W. Interface Nanostructured Array Guided High Performance Electrochemical Actuator. *J. Mater. Chem. A* **2014**, *2* (40), 16836−16841.

(11) Kim, O.; Kim, H.; Choi, U. H.; Park, M. J. One-Volt-Driven Superfast Polymer Actuators Based on Single-Ion Conductors. *Nat. Commun.* **2016**, *7* (1), 13576.

(12) Manzoor, M. T.; Nguyen, V. H.; Umrao, S.; Kim, J. H.; Tabassian, R.; Kim, J. E.; Oh, I. K. Mutually Exclusive p-Type and n-Type Hybrid Electrode of MoS_2 and Graphene for Artificial Soft Touch Fingers. *Adv. Funct. Mater.* **2019**, *29* (48), 1905454.
(13) Tabassian, R.; Kim, J.; Nguyen, V. H.; Kotal, M.; Oh, I. Functionally Antagonistic Hybrid Electrode with Hollow Tubular Graphene Mesh and Nitrogen-Doped Crumpled Graphene for High-Performance Ionic Soft Actuators. *Adv. Funct. Mater.* **2018**, *28* (5), 1705714.
(14) Lu, C.; Yang, Y.; Wang, J.; Fu, R.; Zhao, X.; Zhao, L.; Ming, Y.; Hu, Y.; Lin, H.; Tao, X.; et al. High-Performance Graphdiyne-Based Electrochemical Actuators. *Nat. Commun.* **2018**, *9* (1), 752.
(15) Kotal, M.; Kim, J.; Kim, K. J.; Oh, I. K. Sulfur and Nitrogen Co-Doped Graphene Electrodes for High-Performance Ionic Artificial Muscles. *Adv. Mater.* **2016**, *28* (8), 1610−1615.
(16) Wu, G.; Wu, X.; Xu, Y.; Cheng, H.; Meng, J.; Yu, Q.; Shi, X.; Zhang, K.; Chen, W.; Chen, S. High-Performance Hierarchical Black-Phosphorous-Based Soft Electrochemical Actuators in Bioinspired Applications. *Adv. Mater.* **2019**, *31* (25), 1806492.
(17) Pang, D.; Alhabeb, M.; Mu, X.; Dall'Agnese, Y.; Gogotsi, Y.; Gao, Y. Electrochemical Actuators Based on Two-Dimensional $Ti_3C_2T_x$ (MXene). *Nano Lett.* **2019**, *19* (10), 7443−7448.
(18) Umrao, S.; Tabassian, R.; Kim, J.; Nguyen, V. H.; Zhou, Q.; Nam, S.; Oh, I. MXene Artificial Muscles Based on Ionically Cross-Linked $Ti_3C_2T_x$ Electrode for Kinetic Soft Robotics. *Sci. Robot.* **2019**, *4* (33), No. eaaw7797.
(19) Garai, M.; Mahato, M.; Nam, S.; Kim, E.; Seo, D.; Lee, Y.; Nguyen, V. H.; Oh, S.; Sambyal, P.; Yoo, H.; et al. Metal Organic Framework-MXene Nanoarchitecture for Fast Responsive and Ultra-Stable Electro-Ionic Artificial Muscles. *Adv. Funct. Mater.* **2023**, *33* (10), 2212252.
(20) Kotal, M.; Tabassian, R.; Roy, S.; Oh, S.; Oh, I. K. Metal-Organic Framework-Derived Graphitic Nanoribbons Anchored on Graphene for Electroionic Artificial Muscles. *Adv. Funct. Mater.* **2020**, *30* (29), 1910326.
(21) Liu, L.; Wang, C.; Wu, Z.; Xing, Y. Ultralow-Voltage-Drivable Artificial Muscles Based on A 3D Structure MXene-PEDOT:PSS/AgNWs Electrode. *ACS Appl. Mater. Interfaces* **2022**, *14* (16), 18150−18158.
(22) Wang, F.; Li, Q.; Park, J. O.; Zheng, S.; Choi, E. Ultralow Voltage High-Performance Bioartificial Muscles Based on Ionically Crosslinked Polypyrrole-Coated Functional Carboxylated Bacterial Cellulose for Soft Robots. *Adv. Funct. Mater.* **2021**, *31* (13), 2007749.
(23) Lu, C.; Huang, Q.; Chen, X. High-Performance Silicon Nanocomposite Based Ionic Actuators. *J. Mater. Chem. A* **2020**, *8* (18), 9228−9238.
(24) Nguyen, V. H.; Kim, J.; Tabassian, R.; Kotal, M.; Jun, K.; Oh, J. H.; Son, J. M.; Manzoor, M. T.; Kim, K. J.; Oh, I. K. Electroactive Artificial Muscles Based on Functionally Antagonistic Core-Shell Polymer Electrolyte Derived from PS-b-PSS Block Copolymer. *Adv. Sci.* **2019**, *6* (5), 1801196.
(25) Kotal, M.; Kim, J.; Tabassian, R.; Roy, S.; Nguyen, V. H.; Koratkar, N.; Oh, I. Highly Bendable Ionic Soft Actuator Based on Nitrogen-Enriched 3D Hetero-Nanostructure Electrode. *Adv. Funct. Mater.* **2018**, *28* (34), 1802464.
(26) Kim, O.; Shin, T. J.; Park, M. J. Fast Low-Voltage Electroactive Actuators Using Nanostructured Polymer Electrolytes. *Nat. Commun.* **2013**, *4* (1), 2208.
(27) Roy, S.; Kim, J.; Kotal, M.; Tabassian, R.; Kim, K. J.; Oh, I. K. Collectively Exhaustive Electrodes Based on Covalent Organic Framework and Antagonistic Co-Doping for Electroactive Ionic Artificial Muscles. *Adv. Funct. Mater.* **2019**, *29* (17), 1900161.
(28) Sambyal, P.; Mahato, M.; Taseer, A. K.; Yoo, H.; Garai, M.; Nguyen, V. H.; Ali, S. S.; Oh, I. K. Magnetically and Electrically Responsive Soft Actuator Derived from Ferromagnetic Bimetallic Organic Framework. *Small* **2023**, *19* (23), 2207140.
(29) Mahato, M.; Hwang, W. J.; Tabassian, R.; Oh, S.; Nguyen, V. H.; Nam, S.; Kim, J. S.; Yoo, H.; Taseer, A. K.; Lee, M. J.; et al. A Dual-Responsive Magnetoactive and Electro-Ionic Soft Actuator Derived from A Nickel-Based Metal-Organic Framework. *Adv. Mater.* **2022**, *34* (35), 2203613.
(30) Mahato, M.; Tabassian, R.; Nguyen, V. H.; Oh, S.; Nam, S.; Hwang, W.; Oh, I. CTF-Based Soft Touch Actuator for Playing Electronic Piano. *Nat. Commun.* **2020**, *11* (1), 5358.
(31) Pan, X.; Lan, L.; Di, Q.; Yang, X.; Zhang, H. Acidichromic Organic Crystals with Manifold Mechanical Deformations for Reconfigurable Flexible Optical Tuner. *Wearable Electronics* **2024**, *1*, 111−118.
(32) Wang, C.; Liu, Y.; Guo, Y. Intrinsically Flexible Organic Phototransistors for Bioinspired Neuromorphic Sensory System. *Wearable Electronics* **2024**, *1*, 41−52.
(33) Yang, D.; Kong, X.; Ni, Y.; Ren, Z.; Li, S.; Nie, J.; Chen, X.; Zhang, L. Ionic Polymer-Metal Composites Actuator Driven by the Pulse Current Signal of Triboelectric Nanogenerator. *Nano Energy* **2019**, *66*, 104139.
(34) Nguyen, V. H.; Tabassian, R.; Oh, S.; Nam, S.; Mahato, M.; Thangasamy, P.; Rajabi-Abhari, A.; Hwang, W.; Taseer, A. K.; Oh, I. Stimuli-Responsive MXene-Based Actuators. *Adv. Funct. Mater.* **2020**, *30* (47), 1909504.
(35) Chen, S.; Tan, S. F.; Singh, H.; Liu, L.; Etienne, M.; Lee, P. S. Functionalized MXene Films with Substantially Improved Low-Voltage Actuation. *Adv. Mater.* **2024**, *36*, 2307045.
(36) Wang, B.; Huang, P.; Li, B.; Wu, Z.; Xing, Y.; Zhu, J.; Liu, L. Carbon-Based Nanomaterials Electrodes of Ionic Soft Actuators: from Initial 1D Structure to 3D Composite Structure for Flexible Intelligent Devices. *Small* **2023**, *19* (50), 2304246.
(37) Liu, L.; Su, L.; Lu, Y.; Zhang, Q.; Zhang, L.; Lei, S.; Shi, S.; Levi, M. D.; Yan, X. The Origin of Electrochemical Actuation of MnO_2/Ni Bilayer Film Derived by Redox Pseudocapacitive Process. *Adv. Funct. Mater.* **2019**, *29* (8), 1806778.
(38) Khan, A.; Alamry, K. A.; Jain, R. K. Polypyrrole Nanoparticles-Based Soft Actuator for Artificial Muscle Applications. *RSC Adv.* **2019**, *9* (68), 39721−39734.
(39) Inamuddin; Abbas Kashmery, H. Polyvinylidene Fluoride/Sulfonated Graphene Oxide Blend Membrane Coated with Polypyrrole/Platinum Electrode for Ionic Polymer Metal Composite Actuator Applications. *Sci. Rep.* **2019**, *9* (1), 9877.
(40) Li, H.; Wu, Z.; Xing, Y.; Li, B.; Liu, L. Photoelectric Synergistic Response Properties of the $Ti_3C_2T_x$ MXene-CNT/PDMS Bilayer Actuator. *Nano Energy* **2022**, *103* (A), 107821.
(41) Kiyohara, K.; Sugino, T.; Asaka, K. Molecular Mechanism of Ionic Electroactive Polymer Actuators. *Smart Mater. Struct.* **2011**, *20* (12), 124009.
(42) Ye, H.; Wang, D.; Wu, J.; Yue, Y.; Zhou, Y. Forward and Inverse Kinematics of A 5-DOF Hybrid Robot for Composite Material Machining. *Robot. Cim-Int. Manuf.* **2020**, *65*, 101961.
(43) Xu, Y.; Yang, F.; Mei, Y.; Zhang, D.; Zhou, Y.; Zhao, Y. Kinematic, Workspace and Force Analysis of A Five-DOF Hybrid Manipulator R(2RPR)R/SP+RR. *Chin. J. Mech. Eng.* **2022**, *35* (1), 123.
(44) Yin, G.; Yu, M.; Tong, X.; Wu, Y.; Tian, C.; Li, Y. Fabrication and Performance Analysis of High-Performance Cylindrical Ionic Polymer-Metal Composite Actuators with Various Diameters. *Smart Mater. Struct.* **2022**, *31* (11), 115003.
(45) Sui, M.; Ouyang, Y.; Jin, H.; Chai, Z.; Wei, C.; Li, J.; Xu, M.; Li, W.; Wang, L.; Zhang, S. A Soft-Packaged and Portable Rehabilitation Glove Capable of Closed-Loop Fine Motor Skills. *Nat. Mach. Intell.* **2023**, *5* (10), 1149−1160.

https://doi.org/10.1021/acsomega.4c04647
ACS Omega 2024, 9, 42814−42821